

## AJKFLUIDS2019-4964

### DISCRETE VORTEX MODELING OF A FLAPPING FOIL WITH ACTIVATED LEADING EDGE MOTION

Michael W. Prier    James A. Liburdy\*  
Department of Mechanical Engineering  
Oregon State University  
Corvallis, Oregon 97331

#### ABSTRACT

*Energy harvesting performance for a flapping foil device is evaluated to determine how activated leading edge motion affects the aerodynamic forces and the cycle power generated. Results are obtained for a thin flat foil that pitches about the mid-chord and operates in the reduced frequency range of  $k = fc/U$  of 0.06 - 0.10 and Reynolds numbers of 20,000 and 30,000 with a pitching amplitude of  $70^\circ$  and heaving amplitude of  $h_0 = 0.5c$ . Time resolved data are presented based on direct force measurements and are used to determine overall cycle efficiency and coefficient of power. These results are compared against a panel-based discrete vortex model to predict power production. The model incorporates a leading edge suction parameter predictor for vortex shedding and empirical adjustments to circulatory forces. It is found that the leading edge motions that reduce the effective angle of attack early in a flapping stroke generate larger forces later in the stroke. Consequently, the energy harvesting efficiencies and power coefficients are increased since the generated aerodynamic loads are better synchronized with the foil motion. The efficiency gains are reduced with increasing reduced frequencies.*

#### INTRODUCTION

Flapping foil energy harvesters consist of airfoils or hydrofoils that harvest energy by utilizing fluid forces generated by a sinusoidal flapping motion similar to that seen in nature. These unsteady airfoils typically reach large angles of attack at which flow separation occurs at the leading edge and a large vortex

structure forms. This vortex structure, known as a leading edge vortex, has a low pressure core and therefore can temporarily augment the lift force while it is developing and close to the airfoil. The formation of the LEV is highly nonlinear and is an ongoing research topic as it directly affects the efficiency of flapping foil energy harvesters as well as flapping foil propulsion systems.

The airfoil undergoes sinusoidal flapping motion with rotational pitch  $\theta_p$  and translational heave  $h$  where pitch leads heave in phase by  $90^\circ$ . Positive pitch is clockwise and the beginning of the stroke is the top of the heave. The motion is shown in Figure 1 and is given by

$$\theta_p = -\theta_0 \sin(\omega t) \quad (1)$$

$$h = h_0 \cos(\omega t). \quad (2)$$

For foils with relative leading edge motion, effective angle of attack is defined so as to account for both the motion of the airfoil in the fluid as shown in Figure 1 as well as the effective chord line drawn between the leading and trailing edges as shown in Figure 2.

$$\alpha_{eff} = \theta_p + \beta - \arctan\left(\frac{\dot{h}}{U_\infty}\right). \quad (3)$$

\*Address all correspondence to this author.

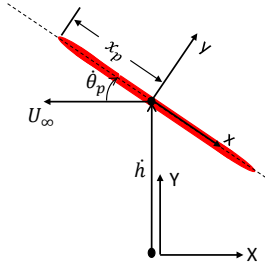


**FIGURE 1.** AIRFOIL MOTION IN THE INERTIAL FRAME  $(X, Y)$  WITH THE COORDINATE SYSTEM  $(x, y)$  ALIGNED WITH THE FOIL CHORD.

A cycle averaged feathering parameter that takes into account the effect of leading edge motion on global effective angle of attack is defined as

$$\chi^* = \frac{1}{T} \int_0^T \frac{\theta_p + \beta}{\arctan(h/U_\infty)} dt \quad (4)$$

where  $T$  is the cycle period. The reduced frequency  $k$  is given by

$$k = fc/U_\infty \quad (5)$$

where  $f$  is the physical frequency, and  $c$  is the rigid chord length. As  $k \rightarrow 0$  the foil becomes quasi-steady, and as  $k \rightarrow \infty$  the operation approaches flapping in quiescent air. For high pitching amplitudes, high reduced frequencies suppress flow separation [1]. The coefficient of lift is given by

$$C_Y = \frac{2F_Y}{\rho U_\infty^2 cb} \quad (6)$$

where  $F_Y$  is the force in the  $y$  direction parallel to the heave translation,  $\rho$  is the fluid density, and  $b$  is the span. The instantaneous power is given by

$$P = \dot{h}F_Y + \dot{\theta}_p M \quad (7)$$

where  $M$  is the moment. For flapping foils operating in the low reduced frequency range the contribution from pitch is secondary and the power is taken as the heave component [2]. The

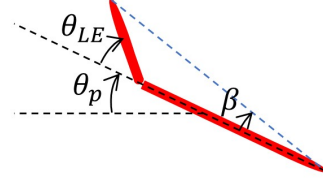


**FIGURE 2.** CAMBER INDUCED BY LEADING EDGE.

cycle averaged power is defined by integrating the instantaneous power over the cycle

$$\bar{P} = \frac{1}{T} \int_0^T P dt \quad (8)$$

and the efficiency is based off of the energy extracted from the fluid verses the fluid energy flowing through the swept area.

$$\eta = \frac{\bar{P}}{P_{fluid}} = \frac{\bar{P}}{\frac{1}{2}\rho U_\infty^3 bd}. \quad (9)$$

## BACKGROUND

A synopsis of the current research on oscillating airfoils in the energy harvesting regime is given here and is a concise version of that presented in Prier [3]. Kinsey and Dumas [2] conducted a parametric study where they identified an optimal reduced frequency range of  $k = 0.12 - 0.18$ . Later studies confirmed this result [4–6]. Unsteady airfoils operating in the low reduced frequency range experience flow separation and LEV formation early in the stroke [1, 7–10]. McKinney and Delaerier [11] conducted the first flapping foil energy harvesting study at a fixed pitch amplitudes of  $25^\circ$  and  $30^\circ$  but since then both Kinsey [2] and Zhu [4] have found that pitch amplitudes of  $70 - 80^\circ$  are optimal.

Trapezoidal pitch profiles are beneficial at low pitch amplitudes [12] but not at high amplitudes which have been determined to be optimal for energy harvesting [13]. Flapping motions where the heave leads the pitch [14] and the pivot point for the main pitch is moved behind the chord have also been tested [15].

Researchers have looked at both leading edge shape and leading edge motion. Rival et al. [16] found that sharp leading edges promote LEV formation earlier but do not greatly impact energy harvesting performance. Liu et al. [17] investigated flexibility at the leading edge based on a trout dorsal fin as well as flexibility at the trailing edge based on a hawkmoth wing for low pitching amplitudes. Tian et al [18] tested flexibility at both the leading edge and over the entire foil. Totpal [7] tested a passively flexible leading edge that moves based on the foil inertia.

Hoke et al. [19] looked at how time varying camber with a constant chord length affected the energy harvesting performance. In addition flexibility at the trailing edge, both discrete and continuous have been found to be beneficial [20–22]. Gueney flaps, both static and time varying also can improve performance [23].

Real world implementation has also been investigated. Kinsey and Dumas [24] applied a turbulence model for foils operating at a Reynold's number of  $Re = 500,000$ . 3D effects have also been explored by Kinsey and Dumas [25] and Deng et al. [26]. Deng [26] looked at how the inertia of the foil would impact real world energy harvesters and Kinsey et al [27] tested a prototype turbine on a pontoon boat. Cho et al [28] studied how performance varies between a uniform freestream and a shear flow.

The research presented here further explores how active control on the leading edge would affect energy harvesting performance in the low reduced frequency range where the foil does not operate at peak performance. While previous studies have found that passive flexibility and active control on the leading edge can be beneficial, the effect of leading edge motion phase for a flapping foil device operating in the energy harvesting regime has not been explored extensively. This research aims to provide more insight into this problem using an experimental flapping device with an actuated leading edge mechanism. In addition a low order discrete vortex method is applied to the flapping motions studied here to determine whether the mechanisms in the model are appropriate for this parameter space.

## POTENTIAL FLOW MODEL FORMULATION

Here an infinitely thin airfoil is modeled using point vortices with vortex shedding at the leading and trailing edges; all calculations are done in the foil frame. Additional details on the model formulation can be found in Prier [3]. The foil translates to the left with velocity  $U_\infty$ , heaves up and down with velocity  $\dot{h}$ , and pitches about the point  $x_p$  measured from the leading edge as shown in Figure 1.

The vortices are placed at the 1/4 panel length and the collocation point at which impermeability is enforced is placed at the 3/4 panel length so as to implicitly satisfy the Kutta condition at the trailing edge. Impermeability is enforced at each collocation point on  $n$  panels via  $n$  linear equations as given in Eqn 10

$$\Sigma A_{ij}\Gamma_j = U_{\infty,n,i} + \dot{h}_{n,i} + (\dot{\theta}_p \times \vec{r}_i)_n - \left( \frac{\partial \Phi_{LEV}}{\partial n} \right)_i - \left( \frac{\partial \Phi_{TEV}}{\partial n} \right)_i \quad (10)$$

where  $n$  denotes the normal direction on each panel  $i$ .  $\dot{h}_{n,i}$  is the velocity contribution from the heave motion,  $(\dot{\theta}_p \times \vec{r}_i)_{n,i}$  is

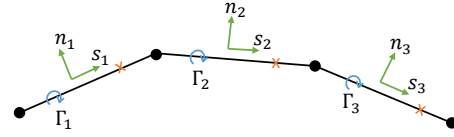


FIGURE 3. AIRFOIL DISCRETIZATION INTO PANELS.

from the pitch, and  $-\left( \frac{\partial \Phi_{LEV}}{\partial n} \right)_i$  and  $-\left( \frac{\partial \Phi_{TEV}}{\partial n} \right)_i$  are the velocity contributions from the previously shed vortices at the leading edge and trailing edge respectively;  $\Phi$  is a perturbation velocity potential from the denoted shed vortices.  $\Sigma A_{ij}\Gamma_j$  is the velocity contribution from the bound vortices on the foil where  $A_{ij}$  is the influence coefficient for vortex  $j$  on collocation point  $i$  and  $\Gamma_j$  are the bound vortex strengths which are being solved for. The influence coefficients for the point vortices are given shortly in Eqn 15 and 16.

The vortex shedding mechanism at the leading edge is taken from Ramesh [29] where the bound circulation is formulated as a Fourier series and vorticity is shed at the leading edge so as to limit the suction at the leading edge. The first Fourier coefficient,  $A_0$ , is taken as a non-dimensional measure of vorticity at the leading edge and will be called the leading edge suction parameter (LESP) [29]. A critical LESP value,  $LESP_{crit}$ , is determined for a particular airfoil at a particular Reynolds number and vortices are shed at the leading edge so as to limit the instantaneous LESP from exceeding this critical value. From Katz and Plotkin [30]  $A_0$  is given by

$$A_0 = -\frac{1}{\pi} \int_0^\pi \frac{W(x,t)}{U_\infty} dv \quad (11)$$

where  $v = 0$  is the leading edge and  $v = \pi$  is the trailing edge in polar coordinates;  $W(x,t)$  is the downwash and is the velocity contributions from the shed vortices and the foil motion

$$W(x,t) = -\left( -U_{\infty,n,i} - \dot{h}_{n,i} - (\dot{\theta}_p \times \vec{r}_i)_n + \left( \frac{\partial \Phi_{LEV}}{\partial n} \right)_i + \left( \frac{\partial \Phi_{TEV}}{\partial n} \right)_i \right). \quad (12)$$

Only the LESP criteria is based on this Fourier series representation since here the bound vorticity is modeled using point

vortices. From Kelvin's circulation theorem the sum of all vorticity must always be zero

$$f(\Gamma)_k = \sum_i \Gamma_i + \sum_{j=1}^{m-1} \Gamma_{j,TEV} + \Gamma_{m,k} + \sum_{j=1}^{q-1} \Gamma_{j,LEV} + \Gamma_{q,k} = 0 \quad (13)$$

where  $\Gamma_{m,k}$  and  $\Gamma_{q,k}$  are the most recently shed vortices from the trailing and leading edge respectively. The vorticity is shed at the leading edge so as to limit the leading edge suction parameter to a critical value both for positive and negative angles of attack

$$f(LESP) = \begin{cases} LESP(t) - LESP_{crit} & LESP > 0 \\ LESP(t) + LESP_{crit} & LESP < 0 \end{cases} \quad (14)$$

These two conditions are met iteratively using a 2D Newton's method. All shed vortices are assumed to convect with the inviscid velocity as calculated from the freestream, bound vorticity, and shed vorticity. The influence coefficients for a point vortex with all the vorticity contained at the vortex location for the x and y direction respectively are

$$u_v = \frac{1}{2\pi} \frac{x - x_v}{\sqrt{(x - x_v)^2 + (y - y_v)^2}} \quad (15)$$

$$v_v = \frac{1}{2\pi} \frac{y - y_v}{\sqrt{(x - x_v)^2 + (y - y_v)^2}} \quad (16)$$

Point vortices are used to represent the bound vorticity on the foil panels. For vortices that are shed the vortex blob model from Vatisas [31] is used; the core radius  $r_{core} = 1.3U_\infty \Delta t$  is used as proposed by Leonard [32] and used by Ramesh [29]. The force is calculated via the vortex impulse method documented by Li [33], [34] and Bai [35] which here reduces to

$$\begin{aligned} F_Y = & \rho \Gamma_b \left( U_\infty - \frac{dx_b}{dt} \right) - \rho x_b \frac{d\Gamma_b}{dt} + \\ & \rho \Gamma_{LEV} \left( U_\infty - \frac{dx_{LEV}}{dt} \right) - \rho x_{LEV} \frac{d\Gamma_{LEV}}{dt} + \\ & \rho \Gamma_{TEV} \left( U_\infty - \frac{dx_{TEV}}{dt} \right) - \rho x_{TEV} \frac{d\Gamma_{TEV}}{dt}. \end{aligned} \quad (17)$$

where  $U_\infty$  is the freestream from the foil's perspective (here going from left to right in the X direction) and  $x_i$  is the X-position

(inertial frame) of each vortex; b subscript denotes bound circulation, LEV subscript denotes vortices shed from the leading edge, and TEV denotes vortices shed from the trailing edge. The 1st, 3rd, and 5th terms are vortex lift terms and make up the circulatory and suction contributions to force. The 2nd, 4th, and 6th terms constitute the unsteady terms or non-circulatory contributions. In classical aerodynamics the circulatory force comes from the bound circulation and the suction force results from the flow navigating 180 degrees around an infinitely thin leading edge. To be explicit the circulatory and suction force in the Y direction are given by

$$\begin{aligned} F_{C,Y} + F_{S,Y} = & \rho \Gamma_b \left( U_\infty - \frac{dx_b}{dt} \right) + \rho \Gamma_{LEV} \left( U_\infty - \frac{dx_{LEV}}{dt} \right) + \\ & \rho \Gamma_{TEV} \left( U_\infty - \frac{dx_{TEV}}{dt} \right) \end{aligned} \quad (18)$$

and the non-circulatory force is given by

$$F_{NC,Y} = -\rho x_b \frac{d\Gamma_b}{dt} - \rho x_{LEV} \frac{d\Gamma_{LEV}}{dt} - \rho x_{TEV} \frac{d\Gamma_{TEV}}{dt}. \quad (19)$$

Here the trailing edge separation model from Beddoes [36] with some additions from Fan [37] as applied by Liu [38] is used since flow separation at the trailing edge is anticipated. The spirit of this model is to calculate a fictitious separation point along the chord line determined from static airfoil data and adjust the circulatory force to account for this loss of bound circulation. The separation point for a static airfoil is given by

$$f_{0,sep} = \begin{cases} 1 - 0.3 \exp\left(\frac{|\alpha_{eff}| - \alpha_1}{S_1}\right) & |\alpha_{eff}| < \alpha_1 \\ 0.04 + 0.66 \exp\left(\frac{\alpha_1 - |\alpha_{eff}|}{S_2}\right) & |\alpha_{eff}| \geq \alpha_1 \end{cases} \quad (20)$$

where  $\alpha_1$  is the break angle at which the static stall occurs,  $S_1$  describes how the force deviates from the small angle slope, and  $S_2$  describes the stall behavior. The separation point is used in a deficiency coefficient as shown below for both the force in the normal direction and axial direction

$$C_{N,sep} = C_{N,circ} \left( \frac{1 + f_{0,sep}^{1/2}}{2} \right)^2 \quad (21)$$

$$C_{s,sep} = C_s (f_{0,sep})^{1/2}. \quad (22)$$

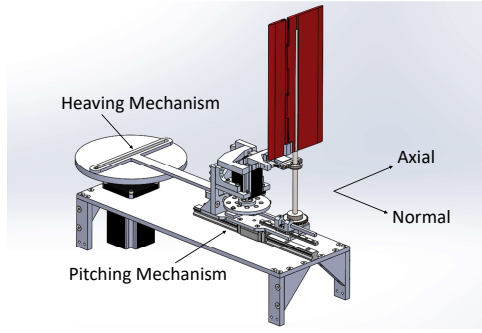


**FIGURE 4.** MODEL OF FLAPPING FOIL DEVICE AND PICTURE OF WING WITH MOTOR INSTALLED.

For the unsteady case a first order lag is applied to account for how the boundary layer reacts to the foil motion

$$\tau_1 \frac{df_{sep}}{dt} + f_{sep} = f_{0,sep}(\alpha_{eff} - \tau_2 \dot{\alpha}_{eff}) \quad (23)$$

where  $\tau_1$  and  $\tau_2$  are empirically determined time constants. For the unsteady case the empirical correction is only applied to the circulatory and suction components, not the non-circulatory part which includes the changing bound circulation and the shedding of vorticity at the leading and trailing edges.

$$C_Y = (C_{N,sep} + C_{N,non}) \cos \theta + C_{s,sep} \sin \theta \quad (24)$$

where  $C_{N,non}$  is the non-circulatory force in the normal direction. The empirical constants used here are taken from Liu [38] for a NACA0015 airfoil:  $S_1 = 3$ ,  $S_2 = 2.3$ ,  $\alpha_1 = 15.25^\circ$ ,  $\tau_1 = 0.52c/U_\infty$ , and  $\tau_2 = 4.5c/U_\infty$ .

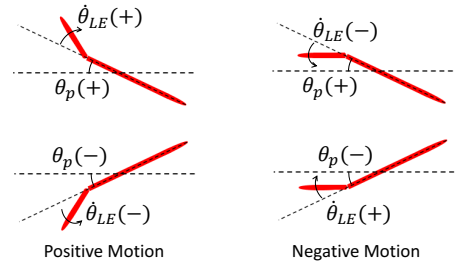


**FIGURE 5.** POSITIVE MOTIONS AND NEGATIVE MOTIONS.

## EXPERIMENTAL SETUP

The experimental setup, experimental procedure, and data reduction are presented in detail in Prier [3] and a concise version is presented here. Force data was collected on a custom built flapping foil device in a recirculating wind tunnel with a test section of  $1.37 \times 1.52m$ . The foil is vertical, eliminating the influence of gravity and situated between endplates so as to minimize 3D effects. A FlowKinetics LLC FKT 3DP1A Manometer was used to determine the freestream velocity. Forces were measured in the drag and lift directions using LSB 200 load cells from Futek. The pitching and heaving motions were generated by G734-1280-4 and G723-400-4 stepper motors from Gecko Drive. The airfoil consists of a titanium rod and 3D printed sections with chord length of  $c = 0.15m$ , a span of  $b = 0.3m$ , and a thickness of  $6.5mm$ . Leading and trailing edges were both elliptical with major to minor axis ratios of 6:1. The motor for controlling the leading edge was a brushed DC Micro Metal Gearmotor HPCB 12V with a 150:1 gear box ratio from Pololu and it was incased in a 3D printed shroud with a thickness of  $14mm$ . An attached magnetic encoder provided position tracking of  $\pm 0.2^\circ$ .

All data was collected at 200Hz using LabVIEW 2013 with a NI PCI-6221. 7-12 trials were conducted for each set point with each trial consisting of more then 70 flapping cycles which were cycle averaged. Since the fluid is air the inertial force from the foil motion is not small compared to the aerodynamic force; Totpal [39] showed that for the current setup that aerodynamic forces from flapping in quiescent air are negligible compared to the aerodynamic force with the wind on. Therefore the inertial force was determined by flapping in quiescent air and was subtracted from the force data with the wind on to leave only the aerodynamic forces of interest.

In testing relative leading edge motions the amplitude of the leading edge displacement was kept constant at  $40^\circ$ ; leading edge amplitude varied slightly with reduced frequency and leading edge motion profiles due to the leading edge inertia and friction in the motor and gearbox. The leading edge motion profiles are trapezoidal with varying phase. Here the motions are char-

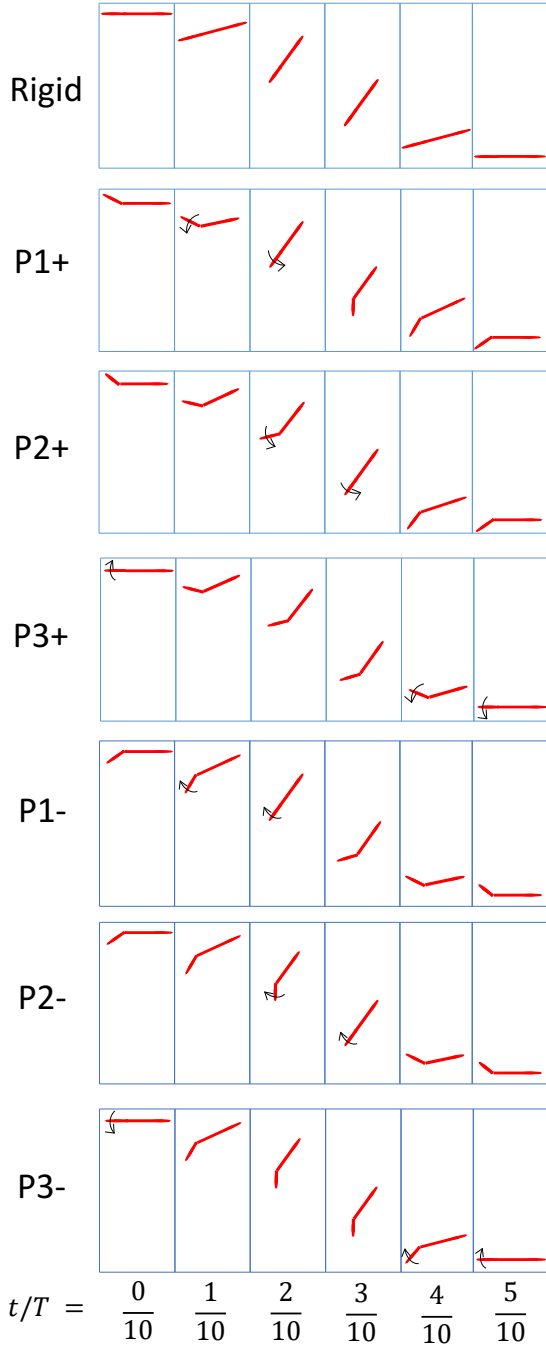


**FIGURE 6.** POSITIVE AND NEGATIVE MOTIONS DURING THE DOWNSTROKE.

acterized as either positive motions or negative motions as seen in Figure 5. Positive motions are motions in which the leading edge has relative velocity  $\dot{\theta}_{LE}$  with the same sign as the instantaneous pitch  $\theta_P$  at the time of initiation; it has no relationship to  $\dot{\theta}_P$ . Positive motions have  $(-)\dot{\theta}_{LE}$  during the downstroke and

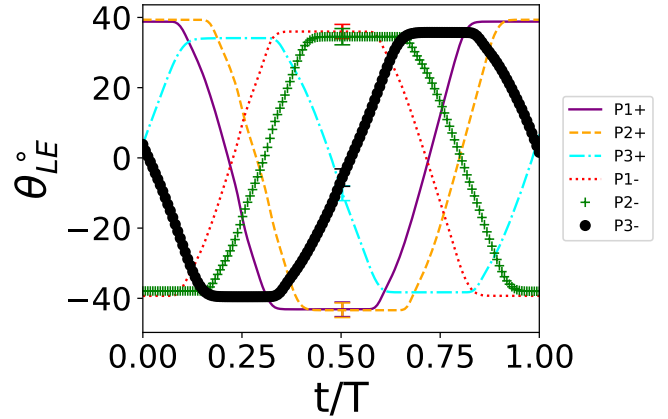


**FIGURE 7.** LEADING EDGE ANGLE FOR THE POSITIVE AND NEGATIVE MOTIONS. CLOCKWISE MOTION IS POSITIVE.

negative motions have  $(+)\dot{\theta}_{LE}$  during the downstroke.

There are three positive motions P1+, P2+, P3+ and three negative motions P1-, P2-, P3-; again the only difference is the phase of the motion and P1+ and P1- have the same motor activation time but they actuate in opposite directions. An illustration of these motions for the downstroke is shown in Figure 6 where the rotational arrows denote instantaneous  $\dot{\theta}_{LE}$ . Plots of  $\theta_{LE}$  for  $k = 0.06$  are shown in Figure 7 where clockwise  $\theta_{LE}$  is considered positive. The differences in the motion between reduced frequencies are small. P3+ and P3- are unique in that the motor activates very late in the stroke and the motion finishes early in the next stroke.

## RESULTS

Force measurements from the wind tunnel were collected in order to determine the theoretical energy harvesting efficiency. Critical LESP values were determined from these force measurements for the model, which will be explained shortly, and the force predictions from the model were compared against the experimental data. All results are from Prier [3].

### Experimental Results

First the wind tunnel force measurements will be presented and the efficiency will be analyzed based on the positive and negative motion characterizations as well as the the cycle averaged feathering parameter  $\chi^*$ .

**Rigid Case** Effective angle of attack, coefficient of lift, and heaving coefficient of power are shown in Figure 8 for the rigid cases. The beginning of the cycle is at the top of the heave. As reduced frequency increases effective angle of attack

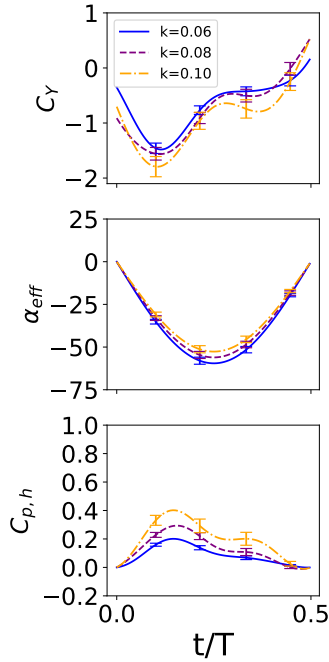


FIGURE 8. RIGID DATA FOR  $k = 0.06, 0.08,$  AND  $0.10$ .

decreases. The force curves all have the same generic shape; the force starts slightly negative, decreases down to a primary peak or local minimum at  $t/T = 0.1$ , then increases up to a saddle at  $t/T = 0.3$  before approaching zero at the end of the stroke. The primary peak at  $t/T = 0.1$  is comparable across the reduced frequencies with a value of  $C_Y = -1.5$ . For  $k = 0.06$  and  $0.08$ , the secondary peak at  $t/T = 0.3$  shows a saddle with  $C_Y = -0.7$  while for  $k = 0.10$  it is a secondary peak with a value of  $C_Y = -0.9$ . The power coefficients are positive for most of the cycle across all reduced frequencies and larger reduced frequencies yield larger power coefficients; at  $t/T = 0.15$ ,  $C_{p,h} = 0.2, 0.3,$  and  $0.4$  for  $k = 0.06, 0.08,$  and  $0.10$  respectively.

**Positive Motions** Effective angle of attack, lift coefficient, and heaving power coefficient are given in Figure 9. P1+ and P2+ start at the same positive  $\alpha_{eff}$  and have the same decreasing profile until  $t/T = 0.1$  when P2+ has a reduced rate of change of  $\alpha_{eff}$ . P3+ starts at  $\alpha_{eff} = 0$  and has the smallest rate of change of effective angle of attack compared to any other motion; it also has the smallest effective angle of attack amplitude. For  $k = 0.06$ , effective angle of attack amplitude is  $70^\circ$  for P1+,  $60^\circ$  for P2+ and the rigid case, and  $50^\circ$  for P3+. The amplitude occurs at  $t/T = 0.25$  for P3+ and the rigid case, and around  $t/T = 0.3$  for P1+ and P2+.

The force curves have the same shape as the rigid cases with a primary peak early in the stroke and smaller forces later in the

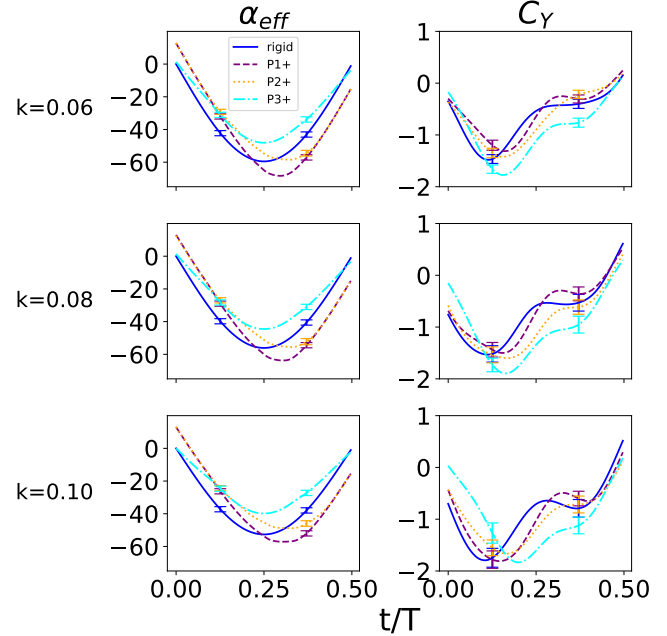


FIGURE 9. EFFECTIVE ANGLE OF ATTACK AND LIFT COEFFICIENT FOR POSITIVE MOTIONS.

stroke. For  $k = 0.06$  P1+, P2+, and P3+ have primary peaks later at  $t/T = 0.15$  while the rigid case occurs at  $t/T = 0.1$ . P3+ has larger forces than the rigid case or P1+ and P2+; P3+ has a primary peak of  $C_Y = -1.7$  while P2+ and the rigid cases have primary peaks of  $C_Y = -1.5$ , and P1+ has a primary peak of  $C_Y = -1.4$ . All the positive motions have larger forces to varying degrees later in the stroke; at  $t/T = 0.23$ ,  $C_Y = -0.8, -1, -1.1,$  and  $-1.4$  for the rigid case, P1+, P2+, and P3+ respectively.

For  $k = 0.10$  the primary force peaks are largely comparable and within each others uncertainty with  $C_Y = -1.75$ ; P3+ has a distinct shift in its primary peak which occurs at  $t/T = 0.2$  compared to the rigid case at  $t/T = 0.1$ . For  $t/T = 0.2 - 0.45$  P3+ has increased force magnitudes compared to any other motion.

The instantaneous heaving power coefficient is given in Figure 10 for the positive motions. For  $k = 0.06$  P3+ has a peak power coefficient at  $t/T = 0.18$  with a value of  $C_{p,h} = 0.3$ ; it has an increased power coefficients from  $t/T = 0.1 - 0.45$  compared to the rigid case. P2+ has a peak power coefficient of  $C_{p,h} = 0.25$  and has larger power coefficients than the rigid case from  $t/T = 0.15 - 0.3$ .

**Negative Motions** Effective angle of attack and lift coefficients are given in Figure 11 for the negative motions. No data was taken at  $k = 0.10$ . P1- and P2- start at negative  $\alpha_{eff}$  and decrease at the same rate up until  $t/T = 0.1$ . Effective angle

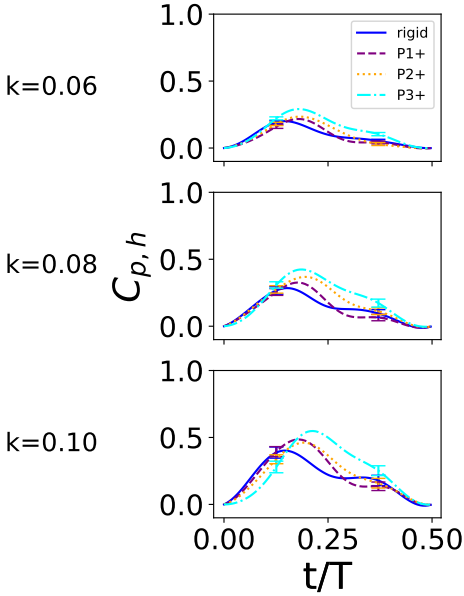


**FIGURE 10.** HEAVING POWER COEFFICIENT FOR THE POSITIVE MOTIONS.

of attack for P3- starts at zero and has the largest rate of change of any motion up until  $t/T = 0.2$ ; P3- has the largest effective angle of attack amplitude and it occurs at  $t/T = 0.25$  which is the same as the rigid case. For  $k = 0.06$ , P1- and the rigid case have  $\alpha_{eff}$  amplitudes of  $50^\circ$ , P2- has an amplitude of  $60^\circ$ , and P3- has an amplitude of  $70^\circ$ . For  $k = 0.08$  the effective angle of attack amplitudes have the same profile and trends but with reduced magnitudes.

The force curves are also shown. For  $k = 0.06$  P1- and P2- have reduced force primary peaks compared to the rigid case with  $C_Y = -1$  around  $t/T = 0.1$ . Later in the stroke P1- and P2- have forces comparable to the rigid case; at  $t/T = 0.35$ ,  $C_Y = -0.6$  for the rigid case and P1- and P2-. P3- has a primary peak comparable to the rigid case at  $t/T = 0.1$  with  $C_Y = -1.5$ . Later in the stroke P3- shows small forces with  $C_Y = -0.2$  at  $t/T = 0.25$ .

The instantaneous power coefficients are shown in Figure 12 for the negative motions. The rigid case shows the largest peak power at  $t/T = 0.15$  with  $C_{p,h} = 0.22$ . Later in the stroke the rigid case, P1-, and P2- have comparable power coefficients of  $C_{p,h} = 0.1$ . P3- has the same instantaneous heaving power as the rigid case up until  $t/T = 0.1$  at which point it decreases and at  $t/T = 0.2$  it is  $C_{p,h} = 0.1$ ; the value does not change for the rest of the stroke.

The heaving efficiency vs the foil motion for each reduced frequency is given in Figure 13. For the rigid case at  $k = 0.06, 0.08, 0.10$  the efficiencies are  $\eta = 6.5\%, 9.5\%,$  and  $13.75\%$  respectively. The negative motions P1-, P2-, and P3- show decreased performance compared to the rigid case; these motions

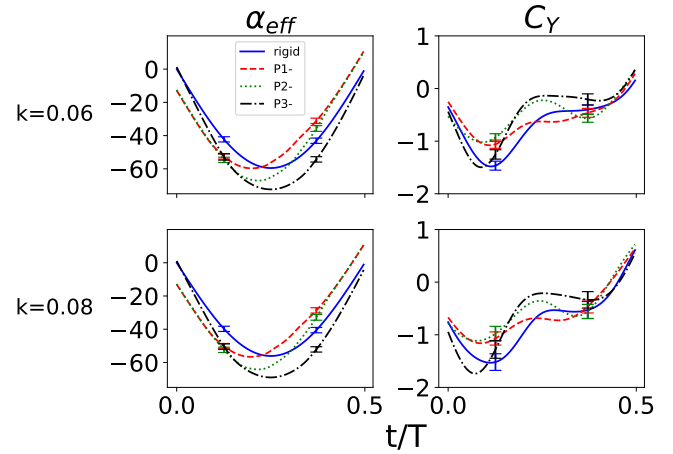


**FIGURE 11.** EFFECTIVE ANGLE OF ATTACK AND LIFT COEFFICIENT FOR NEGATIVE MOTIONS.

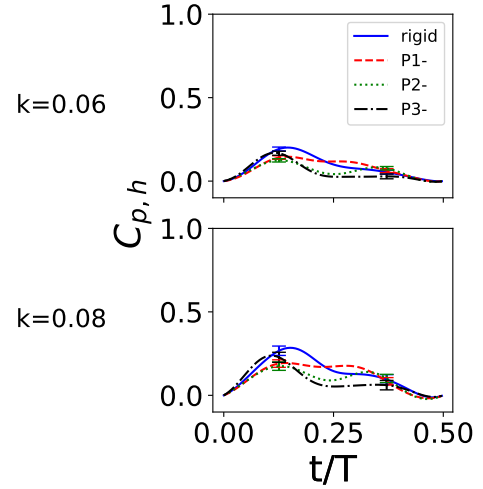


**FIGURE 12.** HEAVING POWER COEFFICIENTS FOR NEGATIVE MOTIONS.

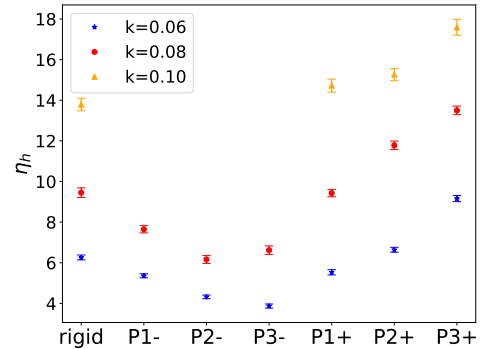


**FIGURE 13.** HEAVING EFFICIENCY VS MOTION.

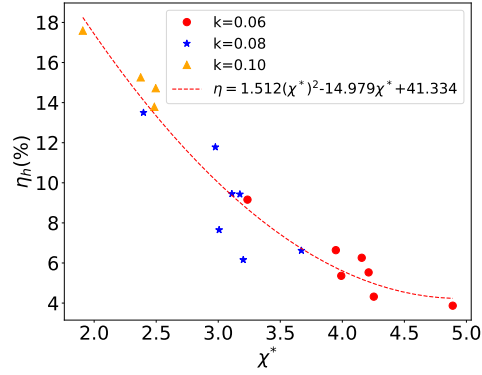


**FIGURE 14.** HEAVING EFFICIENCY VS CYCLE AVERAGED FEATHERING PARAMETER.

have larger effective angles of attack early in the stroke compared to the rigid case. P2+ and P3+ show increased efficiencies compared to the rigid case; for  $k = 0.06$ , P3+ has an efficiency increase of 43% compared to the rigid case and for  $k = 0.10$  the efficiency increases 25% compared to the rigid case.

The heaving efficiency is plotted vs the cycle averaged feathering parameter, which encodes information both on the reduced frequency and the leading edge motion, in Figure 14. The data collapses well on the quadratic curve.

### Model Results

Here the results from the unsteady panel method with vortex shedding at the leading and trailing edges will be presented. First the code is validated against previous work. Appropriate critical LESP values are determined by minimizing the error between the experimental forces and the model forces. Then, model predictions for the lift force are compared directly to the experimental results. Again all results are from Prier [3].

**Validation** The unsteady panel method with vortex shedding at the leading and trailing edges is validated against Ramesh's thin airfoil results [29] and Kinsey's CFD [2] for  $k = 0.14$ ,  $h_0 = c$ ,  $x_p = c/3$ , and  $Re = 1100$  for a NACA0015 airfoil where  $LESP_{crit} = 0.19$ . The lift coefficient is shown in Figure 15. The panel method has small asymmetry between the downstroke and upstroke. The Panel method compares well to the CFD; while the panel method starts near  $C_Y = 1$  at  $t/T = 0$  and the CFD starts at  $C_Y = 0$ , the panel method quickly decreases and converges on the CFD curve. At  $t/T = 0.1$  the CFD has a first force peak of  $C_Y = -1.8$  while the panel method predicts  $C_Y = -2$ . The panel method overpredicts the valley or local maximum at  $t/T = 0.3$  with  $C_Y = -1.5$  where as the CFD shows  $C_Y = -1$ . For the second peak at  $t/T = 0.4$  the panel method predicts  $C_Y = -2$  while the CFD predicts  $C_Y = -1.6$ . The panel method captures the second force peak better than the thin airfoil

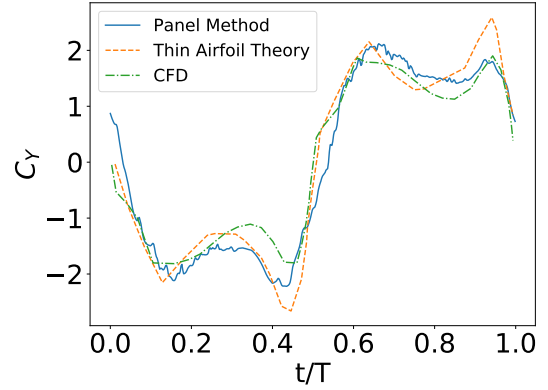


**FIGURE 15.** PANEL METHOD COMPARISON TO THIN AIRFOIL THEORY FROM RAMESH [29] AND CFD FROM KINSEY AND DUMAS [2].

	k=0.06	k=0.08	k=0.10
Rigid	0.08	0.13	0.11
P1+	0.05	0.05	0.24
P2+	0.03	0.19	0.19
P3+	0.08	0.19	0.05
P1-	0.13	0.16	
P2-	0.08	0.16	
P3-	0.11	0.11	

**TABLE 1.** CRITICAL LESP VALUES IDENTIFIED FROM THE ERROR MINIMIZATION PROCESS FOR ALL MOTIONS..

theory.

**Identifying the Appropriate Critical LESP** The preferred method to determine the appropriate critical LESP value is to look for the first instance of vortex shedding at the leading edge from either PIV or CFD. Here neither data is available and instead the model is run for a wide range of critical LESP values and the case that produces the smallest normalized-root-mean-squared (NRMS) error against the experiment is taken as the appropriate value [29]. The range of values tested is  $0 \leq LESP_{crit} \leq 0.4$  with 16 evenly spaced values tested; a moving average with a 3 term window was applied to all the error curves so as to identify a clear critical value for cases in which the NRMS error oscillates near the minimum. Identified critical LESP values for all motions are shown in Table 1.

The appropriate critical LESP value is plotted against the cycle averaged feathering parameter which encodes information

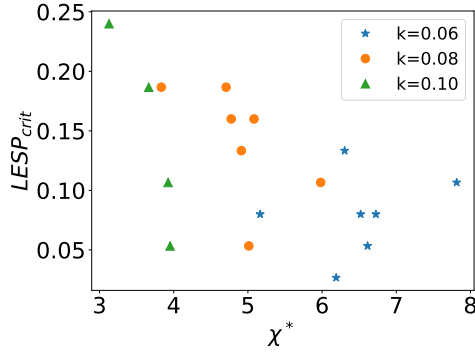


**FIGURE 16.** CRITICAL LESP VALUES VS THE CYCLE AVERAGED FEATHERING PARAMETER.

on both reduced frequency and leading edge motion in Figure 16. There is no clear relationship between the critical LESP value and  $\chi^*$  with the data being scattered. There is a weak trend of critical LESP increasing with increasing reduced frequency but the scatter is large.

**Lift Coefficient Comparison** The lift coefficients from the model are compared against the experimental forces for all motions in Figure 17. DVM is the model prediction without the empirical correction and DVMA is with the empirical correction. For all motions DVMA is not significantly different than DVM; this will be addressed shortly. The model over predicts the lift force almost everywhere for all cases although the timing of the primary peak is roughly correct; for the rigid case at  $k = 0.06$  DVM has  $C_Y = -2.5$  while the experiment has  $C_Y = -1.4$  both at time  $t/T = 0.1$ . For P3+ at  $k = 0.08$  DVM has  $C_Y = -2.5$  while the experiment has  $C_Y = -1.8$  both at time  $t/T = 0.2$ . For P3+ at the highest reduced frequency of  $k = 0.10$  the model has a plateau at  $t/T = 0.17$  with a value of  $C_Y = -2.5$  while the experiment has a clear peak of  $C_Y = -1.75$  at  $t/T = 0.2$ . The P3- motion at  $k = 0.06$  compares very well against the experiment between  $t/T = 0.05 - 0.3$ ; P3- at  $k = 0.08$  compares well against the experiment between  $t/T = 0.1 - 0.4$ . P1- and P2- at  $k = 0.06$  and  $k = 0.08$  compare poorly to the experiments in the first half of the stroke with up to 100% error.

In Figure 18 the circulatory force coefficient and non-circulatory force coefficient are plotted for all motions. The suction force is small due to vortex shedding and therefore ignored. It is clearly seen that the non-circulatory force is dominant and the circulatory force is small. For the rigid case, P1+, P2+, and P3+ the circulatory force is comparable to the non-circulatory force early in the stroke up to  $t/T = 0.08$ . Once vortex shedding at the leading edge begins the non-circulatory force increases and this coincides with the circulatory force decreasing. The peak non-circulatory force coincides with a minimum and sometimes slightly positive circulatory force. For example, the rigid case at

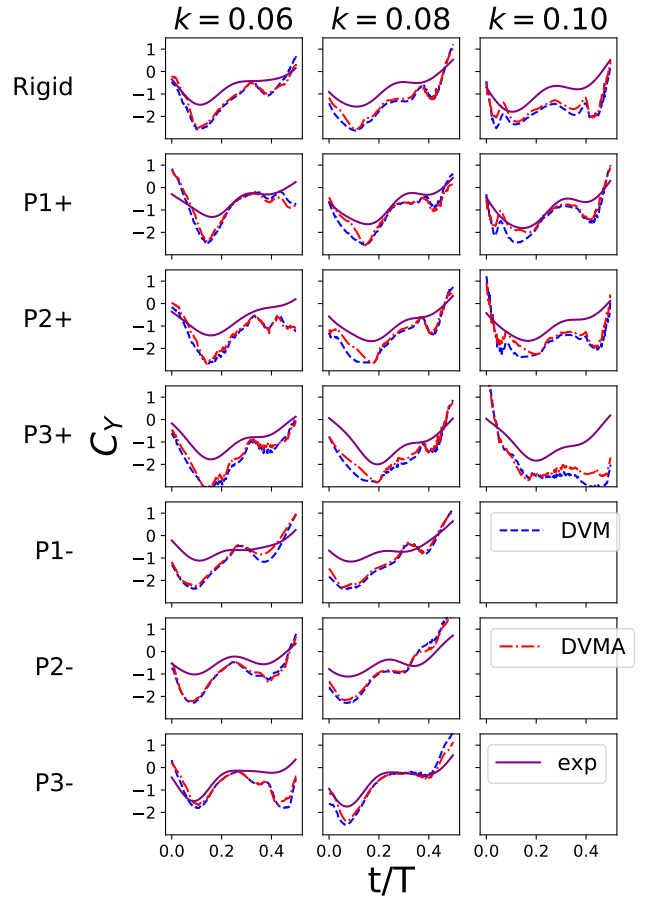


**FIGURE 17.** COMPARISON OF LIFT COEFFICIENT FROM THE MODEL AGAINST THE EXPERIMENTS. DVM IS THE MODEL WITHOUT THE TRAILING EDGE SEPARATION CORRECTION AND DVMA IS THE MODEL WITH THE TRAILING EDGE SEPARATION CORRECTION.

$k = 0.06$  has a peak non-circulatory force of  $-2.25$  at  $t/T = 0.1$  while the circulatory force at this same instant is zero; this trend is seen for all positive motions albeit at varying times and with varying non-circulatory peak values. Interestingly, for the rigid cases the non-circulatory force follows the experimental forces moderately well for  $t/T = 0.1 - 0.4$ . For the positive motions the non-circulatory force has a distinct secondary peak late in the stroke around  $t/T = 0.4$ ; the negative motions show varying behavior with P2- and P3- at  $k = 0.06$  showing secondary non-circulatory force peaks at  $t/T = 0.4$  while the other negative motions have very small non-circulatory forces later in the stroke.

Due to the shortcomings of the model with the current empirical adjustment, the empirical correction was applied to both

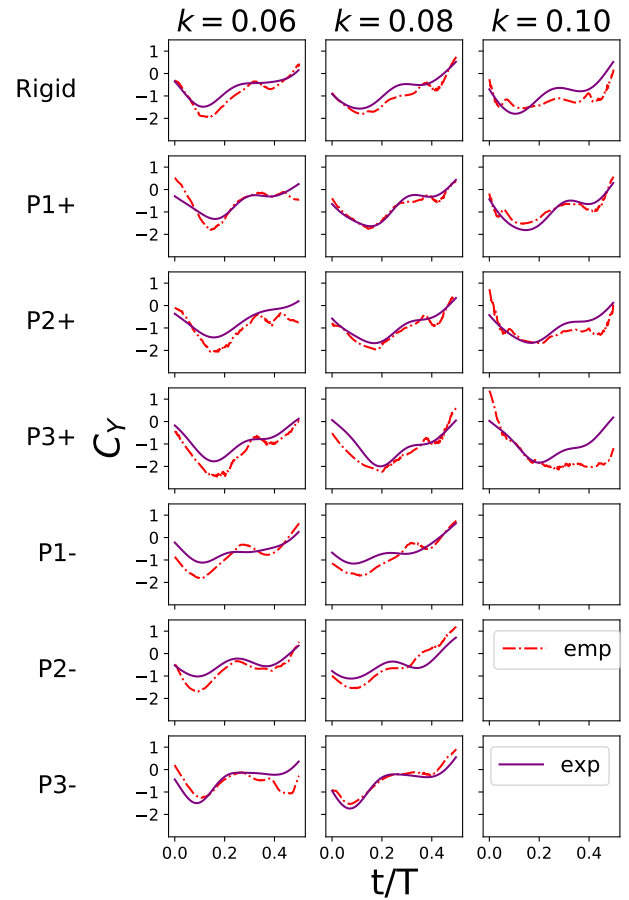
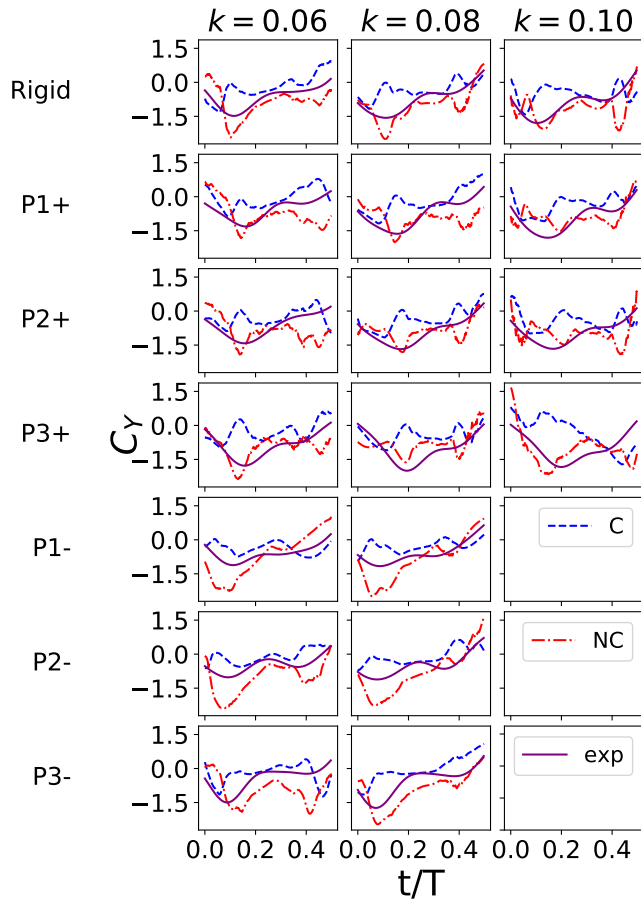


**FIGURE 18.** COMPARISON OF LIFT COEFFICIENT FROM THE MODEL AGAINST THE EXPERIMENTS. NC IS THE NON-CIRCULATORY FORCE AND C IS THE CIRCULATORY FORCE.

**FIGURE 19.** COMPARISON OF LIFT COEFFICIENT FROM THE MODEL WITH THE EMPIRICAL ADJUSTMENT APPLIED TO BOTH THE CIRCULATORY AND NON-CIRCULATORY FORCE (emp). THE EXPERIMENTAL FORCES ARE 'exp'.

the circulatory and non-circulatory force components in Figure 19. This adjusted force curve is designated by 'emp' in Figure 19 and compares well against the experimental results. The shape of the force curve is preserved and it compares better with the model because the magnitudes are further reduced compared to the Leishman-Beddoes model. The model compares exceptionally well to the experiments for  $k = 0.08$  for P1+ and P2+ as well as P1+ at  $k = 0.10$  and P3- at  $k = 0.08$ . The model performs the worst for P3+ at  $k = 0.10$  where it fails to predict the force decrease in the second half of the stroke; interestingly this motion also has the smallest effective angles of attack and produces the largest heaving efficiency. It should be noted that to the author's knowledge there is no justification for applying the empirical correction to the non-circulatory force.

## DISCUSSION

From the experiments it is seen that leading edge motions that have reduced effective angles of attack early in the stroke produce larger forces later in the stroke during higher heaving velocities thus increasing the heaving power. Both P2+ and P3+ have improved heaving efficiencies because their lift forces are better aligned with their heaving velocities. P3+ also has larger primary force peaks than any other motion for  $k = 0.06$  and  $0.08$ . Both smaller effective angle of attack and reduced rate of change of effective angle of attack cause larger lift forces later in the stroke. On the other hand the negative motions have increased effective angle of attack magnitudes early in the stroke and decreased heaving efficiencies. P1- and P2- have stunted force primary peaks while P3- has a primary peak comparable to the rigid case but very small lift force later in the stroke during high  $\alpha_{eff}$ .

These experiments suggest that leading edge motions work to change the entire foil geometry. While no flow visualization was done to determine how the flow evolves with the different leading edge motions, some speculation can be done based off the force curves. Leading edge motions with reduced effective angles of attack have larger forces later in the stroke which might suggest that LEV formation is hindered for these motions and that static stall like conditions are mitigated later in the stroke. P1- and P2- both start at  $\alpha_{eff}$  close to common stall angles which might explain why their primary force peaks are reduced. P3- reaches the largest effective angle of attack of any motion and therefore has significant stall and loss of lift later in the stroke.

It was hypothesized by Ramesh [29] that at high reduced frequencies where flow separation at the trailing edge is largely absent that a given airfoil at a particular Reynolds number would have a critical LESP value that is valid for all airfoil motions. Here the foil operation deviates from these requirements; the foil geometry is changing with time and flow separation at the trailing edge is expected. The appropriate critical LESP value as determined by the error minimization method are scattered against the cycle averaged feathering parameter. All critical LESP values are less than  $LESP = 0.25$  since at this reduced frequency range significant flow separation should occur. There is no clear relationship between appropriate critical LESP and reduced frequency or leading edge motion suggesting that a single critical LESP value is insufficient as a vortex shedding mechanism for flexible foils at low reduced frequencies.

For each appropriate  $LESP$  value the corresponding lift force curves are shown both with and without the trailing edge separation correction. The model without the trailing edge separation is able to capture some generic trends in the force curves such as the location of the primary peak and when the lift force is increasing and decreasing but is inaccurate for predicting the force at any moment in the stroke. Applying the trailing edge separation correction to the circulatory force does not help because the circulatory force is small. The largest force contribution in the model for this parameter range is the non-circulatory force which includes the effect of vortex shedding at the leading edge. Therefore, applying a correction factor to the circulatory force component does not significantly change the predicted forces. Applying the correction to both the circulatory and non-circulatory components improves the accuracy of the model. This might suggest that the model is not accurately predicting the vorticity distribution in the far field, and in particular that too much vorticity is being shed at the leading edge since the non-circulatory force is large. Finally it should be noted that a key goal of a model such as the one presented here is to predict aerodynamic performance and in the case of a wing with a flexible leading edge to predict how leading edge motions would affect the aerodynamic forces; while the model is able to closely match the experimental forces to varying degrees it is not clear that it can reliably predict how a particular leading edge motion

would affect the forces aerodynamic forces.

## CONCLUSION

Force measurements were conducted on a flapping foil with an active leading edge control. It was found that leading edge motions that reduce the effective angle of attack early in the stroke produce larger forces later in the stroke; these larger forces occur during higher heaving velocities thereby increasing the heaving efficiency. Leading edge motions with increased effective angles of attack have reduced forces later in the stroke and it is speculated that this is due to onset of static stall. A cycle averaged feathering parameter that takes into account the leading edge motion is found to correlate well with the heaving efficiency. The experimental results provide insight into a mechanism that could be used to improve flapping foil energy harvesters whose operation deviates from peak conditions. Future work could address how leading edge motions that reduce the effective angle of attack compare to rigid foil operation with reduced pitch amplitude in this low reduced frequency range. Whether the experimental trends presented here continue into the optimal reduced frequency range is also a question. Flow visualization to determine how the LEV formation is affected by leading edge motion would also be of interest. Finally no consideration to the power contribution from the leading edge motion was given and this might affect the conclusion of this work.

A panel method with vortex shedding at the leading edge based on the LESP criteria and with the Kutta condition applied at the trailing edge was implemented for the flapping scenarios. The appropriate critical LESP value for each motion was determined by conducting error minimization between the experimental force curves and a wide range of critical LESP values; it was shown that all critical LESP values were less than  $LESP_{crit} = 0.25$  and that there was no correlation between  $LESP_{crit}$  and the reduced frequency or leading edge motion. The model predictions for force at the appropriate critical LESP values captured generic trends but failed to accurately predict the forces during the stroke. The non-circulatory force contribution dominates in this parameter space making trailing edge separation corrections that apply only to the circulatory force insufficient. Future work should focus on better low order mechanisms for vortex shedding at the leading edge and trailing edge; this could mean an adjusted Kutta condition at the trailing edge or a time varying suction parameter to account for varying foil geometry.

## REFERENCES

- [1] Baik, Y., Bernal, L., Granlund, K., and OI, M., 2012. "Unsteady force generation and vortex dynamics of pitching and plunging aerofoils". *Journal of Fluid Mechanics*, **709**, pp. 37–68.

- [2] Kinsey, T., and Dumas, G., 2008. “Parametric study of an oscillating airfoil in a power-extraction regime”. *American Institute of Aeronautics and Astronautics Journal*, **46**, pp. 1318–1330.
- [3] Prier, M., 2019. “Energy Harvesting Performance of a Flapping Foil with Leading Edge Motion”. Master’s thesis, Oregon State University, Corvallis, Oregon.
- [4] Zhu, Q., 2011. “Optimal frequency for flow energy harvesting of a flapping foil”. *Journal of Fluid Mechanics*, **675**, pp. 495–517.
- [5] Veilleux, J.-C., and Dumas, G., 2017. “Numerical optimization of a fully-passive flapping-airfoil turbine”. *Journal of Fluids and Structures*, **70**, 04, p. 102130.
- [6] Yu, M., and Wang, Z., 2013. “Numerical simulation of oscillating-wing based energy harvest mechanism using the high-order spectral difference method”. *31st AIAA Applied Aerodynamics Conference*, 06.
- [7] Totpal, A. D., Siala, F. F., and Liburdy, J. A., 2018. “Energy harvesting of an oscillating foil at low reduced frequencies with rigid and passively deforming leading edge”. *Journal of Fluids and Structures*, **82**, pp. 329–342.
- [8] Siala, F., W. Prier, M., and Liburdy, J., 2018. “Force production mechanisms of a heaving and pitching foil operating in the energy harvesting regime”. p. V001T07A002.
- [9] Kim, D., Strom, B., Mandre, S., and Breuer, K., 2017. “Energy harvesting performance and flow structure of an oscillating hydrofoil with finite span”. *Journal of Fluids and Structures*, **70**, pp. 314–326.
- [10] Widmann, A., 2015. “Formation and detachment of leading edge vortices on unsteady airfoils”. PhD thesis, Technische Universitt.
- [11] McKinney, W., and Delaurier, J., 1981. “The wingmill: an oscillating-wing windmill”. *Journal of Energy*, **5**, pp. 109–109.
- [12] Xiao, Q., Liao, W., Yang, S., and Peng, Y., 2011. “How motion trajectory affects energy extraction performance of a biomimic energy generator with an oscillating foil?”. *Renewable Energy*, **37**(1).
- [13] Teng, L., Deng, J., Pan, D., and Shao, X., 2016. “Effects of non-sinusoidal pitching motion on energy extraction performance of a semi-active flapping foil”. *Renewable Energy*, **85**(C), pp. 810–818.
- [14] Xie, Y., Lu, K., and Zhang, D., 2014. “Investigation on energy extraction performance of an oscillating foil with modified flapping motion”. *Renewable Energy*, **63**(1), pp. 550–557.
- [15] Siala, F., and Liburdy, J. A., 2015. “Energy harvesting of a heaving and forward pitching wing with a passively actuated trailing edge”. *Journal of Fluids and Structures*, **57**(C), pp. 1–14.
- [16] Rival, D., Kriegseis, J., Schaub, P., Widmann, A., and Tropea, C., 2014. “Characteristic length scales for vortex detachment on plunging profiles with varying leading-edge geometry”. *Experimental Fluids*, **55**, p. 1660.
- [17] Liu, W., Xiao, Q., and Cheng, F., 2013. “Abio-inspired study on tidal energy extraction with flexible flapping wings”. *Bioinspiration Biomimetics*, **8**(3).
- [18] Tian, F.-B., Young, J., and Lai, J. C., 2014. “Improving power-extraction efficiency of a flapping plate: From passive deformation to active control”. *Journal of Fluids and Structures*, **51**, pp. 384–392.
- [19] Hoke, C., Young, J., and Lai, J., 2015. “Effects of time-varying camber deformation on flapping foil propulsion and power extraction”. pp. 152–176.
- [20] Liu, W., Xiao, Q., and Zhu, Q., 2016. “Passive flexibility effect on oscillating foil energy harvester”. *AIAA Journal*, **54**(1), pp. 1172–1187.
- [21] Wu, J., Shu, C., Zhao, N., and Tian, F.-B., 2015. “Numerical study on the power extraction performance of a flapping foil with a flexible tail”. *Physics of Fluids*, **27**, 01, p. 013602.
- [22] Liu, Z., Tian, F.-B., Young, J., and Lai, J., 2017. “Flapping foil power generator performance enhanced with a spring-connected tail”. *Physics of Fluids*, **29**, 12.
- [23] Zhu, B., Huang, Y., and Zhang, Y., 2018. “Energy harvesting properties of a flapping wing with a adaptive gurney flap”. *Energy*, **152**, 06, pp. 117–128.
- [24] Kinsey, T., and Dumas, G., 2014. “Optimal operating parameters for an oscillating foil turbine at reynolds number 500,000”. *AIAA Journal*, **52**(9), pp. 1885–1895.
- [25] Kinsey, T., and Dumas, G., 2012. “Computational fluid dynamics analysis of a hydrokinetic turbine based on oscillating hydrofoils”. *Journal of Fluids Engineering (Transactions of the ASME)*, **134**(2), pp. 1–16.
- [26] Deng, J., Caulfield, C. P., and Shao, X., 2014. “Effect of aspect ratio on the energy extraction efficiency of three-dimensional flapping foils”. *Physics of Fluids*, **26**(4).
- [27] Kinsey, T., Dumas, G., Lalande, G., Ruel, J., Mhut, A., Viarouge, P., Lemay, J., and Jean, Y., 2011. “Prototype testing of a hydrokinetic turbine based on oscillating hydrofoils”. *Renewable Energy*, **36**(6), pp. 1710–1718.
- [28] Cho, H., and Zhu, Q., 2014. “Performance of a flapping foil flow energy harvester in shear flows”. *Journal of Fluids and Structures*, **51**, pp. 199–210.
- [29] Ramesh, K., Gopalarathnam, A., Granlund, K., Ol, M., and Edwards, J., 2014. “Discrete-vortex method with novel shedding criterion for unsteady aerofoil flows with intermittent leading-edge vortex shedding”. *Journal of Fluid Mechanics*, **751**, pp. 500–538.
- [30] Katz, J., and Plotkin, A., 2001. *Low-Speed Aerodynamics*. Cambridge University Press.
- [31] Vastistas, G., Kozel, V., and Mih, W., 1991. “A simpler model for concentrated vortices”. *Experiments in Fluids*, **11**(1), pp. 73–76.

- [32] Leonard, A., 1980. "Vortex methods for flow simulation". *Journal of Computational Physics*, **37**, pp. 289–335.
- [33] Li, J., and Wu, Z., 2015. "Unsteady lift for the wagner problem in the presence of additional leading/trailing edge vortices". *Journal Of Fluid Mechanics*, **769**, pp. 182–217.
- [34] Li, J., Bai, C.-Y., and Wu, Z.-N., 2015. "A two-dimensional multibody integral approach for forces in inviscid flow with free vortices and vortex production". *Journal of Fluids Engineering, Transactions of the ASME*, **137**, 02.
- [35]
- [36] Beddoes, T. S., 1989. "A semi-empirical model for dynamic stall". *Journal of the American Helicopter Society*, **34**(3), pp. 3–17.
- [37] Fan, Y., 1997. "Identification of an unsteady aerodynamic model up to high angle of attack regime". PhD thesis, Virginia Tech.
- [38] Liu, Z., Lai, J. C. S., Young, J., and Tian, F.-B., 2017. "Discrete vortex method with flow separation corrections for flapping-foil power generators.(author abstract)". *AIAA Journal*, **55**(2).
- [39] Totpal, A., 2017. "The Energy Extraction Performance of an Oscillating Rigid and Flexible Foil". Master's thesis, Oregon State University, Corvallis, Oregon.